Journal of Materials Chemistry A

ROYAL SOCIETY OF CHEMISTRY

PAPER

View Article Online
View Journal | View Issue

Cite this: J. Mater. Chem. A, 2025, 13, 34493

Nanostructured sodium vanadate hydrate as a versatile sodium ion cathode material for use in organic media and for aqueous desalination

Daniel Commandeur, *[a] Vlad Stolojan, [b] Monica Felipe-Sotelo, [a] James Wright, [a] David Watson[a] and Robert C. T. Slade [a]

Received 24th June 2025
Accepted 14th September 2025

DOI: 10.1039/d5ta05128b

rsc.li/materials-a

Sodium vanadate hydrate ($NaV_3O_8 \cdot xH_2O$, NVOH) exhibits a wider interlayer spacing than its anhydrous form (NaV_3O_8, NVO), allowing a greater volume for sodium intercalation and, consequently, a higher specific capacity in sodium-ion batteries (SIBs). However, the presence of H_2O hinders the long-term cycling stability of the material in an organic medium, whereas its application in aqueous media has received significant attention. In this work, the hydrothermal synthesis of NVO is optimised to maximise both sodium and crystalline water content, thereby enhancing battery performance in both organic cells and aqueous desalination cells. When tested within organic half-cells, the optimised structure provided an exceptional specific capacity of 280 mA h g^{-1} at 10 mA g^{-1} and demonstrated cycling stability (150 cycles, > 100 mA h g^{-1}, 100 mA g^{-1}). The performance of this material was confirmed in a full sodium ion battery (SIB) with a C@V_2O_3 counter electrode, yielding 70 mA h g^{-1} at 100 mA g^{-1}. This optimised structure was then measured in a new platform designed to provide low-cost high-throughput three-electrode electrochemical testing. Using NaCl(aq) as the electrolyte verified promise of NVOH for desalination batteries as a sodium extraction anode, showing a high estimated desalination capacity of 173 mg_{NaCl} g^{-1}.

Introduction

The ambitious targets for achieving global net zero emissions by 2050 require innovative electrochemical storage solutions to keep pace with low-cost renewable energy. Lithium-ion batteries (LIBs) are the incumbent technology for domestic and grid-scale electrochemical energy storage. However, LIBs require scarce materials and evoke safety concerns due to their electrolytes.[1] Sodium-ion batteries (SIBs) offer a potential future alternative to LIBs, with comparable specific capacity whilst using earth-abundant ions and electrode materials, and have seen renewed attention recently.[2–4] Despite this, SIBs suffer from low energy density and poor cycling stability,[5] and the complex synthesis required for state-of-the-art cathodes (such as Prussian white)[6] prevents this technology from being the envisioned drop-in replacement of LIBs.[7]

Sodium vanadate (V) (NaV_3O_8, NVO) and its hydrate ($NaV_3O_8 \cdot xH_2O$, NVOH) have been reported as a promising cathode and anode in organic and aqueous SIBs.[8–10] The ease of synthesis by the hydrothermal method enables the scalable production of high-aspect-ratio belt structures, which are well-suited for electrolyte infiltration and, consequently, exhibit reasonable ionic transport.[11–13] Despite this, during application to SIBs, these materials typically exhibit poor cycle stability and rate capability.[14–16] Herein, we present a new solution to this issue, retaining water molecules within the interlayer structure, which improves charge storage capacity, stability, and rate capability. Typically, H_2O is removed through heat treatment of the powders produced by hydrothermal synthesis, due to concerns that H_2O may cause device instability and capacity fade.[17] However, in this work the quantity of interlayer H_2O and Na^+ is controlled through the duration of hydrothermal treatment, revealing insights into the reaction mechanism over 48 hours. Furthermore, water-containing intercalation materials pose less of an issue for aqueous batteries, as NVOH has previously displayed remarkable stability in such systems.[18]

The pressing need for access to clean drinking water is encapsulated in UN Sustainable Development Goal 6, which focuses on ensuring access to clean water and sanitation.[19] In 2022, 703 million people lacked access to basic drinking water. This will become an even more severe problem due to climate change in the coming years, with European river discharges predicted to decline by 40% by 2050, affecting areas where 30% of people already experience water stress each year.[20] Electrochemical desalination of seawater has already shown promise in reducing the salt content towards freshwater use, typically in a continuous flow mode.[21] Previously, Yue *et al.* demonstrated

[a]School of Chemistry and Chemical Engineering, University of Surrey, Guildford GU2 7XH, UK. E-mail: d.commandeur@surrey.ac.uk

[b]Advanced Technology Institute, School of Computer Science and Engineering, University of Surrey, Stag Hill, Guildford GU2 7XH, UK

the potential of NVO on reduced graphene oxide (NVO@rGO) as a deionising electrode against Ag@rGO, with a salt removal capacity of 82.2 mg g^{-1}.[22] Desalination batteries, meanwhile, utilise chloride and sodium storage materials together to reversibly extract salt from solution in charge mode, whilst releasing stored energy during discharge.[23–25] These batteries utilise brine concentrates and seawater as electrolytes, alleviating both much of the cost and safety concerns.

In this work, NVOH is applied for the first time to desalinating batteries, likely removing up to 10 mg cm^{-2} of salt from a brine concentrate (NaCl(aq), 3 mol dm^{-3}) when placed against a graphite rod for chloride extraction. Furthermore, in newly developed high-throughput batch cells, the NVOH displayed > 80 mA h g^{-1} recoverable discharge capacity in a 3-electrode cell against Ag/AgCl (discharging from – 1 to 0 $V_{Ag/AgCl}$) and reversible capacity up to 1000 cycles. Not only this but in organic medium half-cells, the strategy of retaining crystal interlayer water yielded a specific capacity of 280 mA h g^{-1} at 10 mA g^{-1}, one of the highest capacities reported for SIB cathodes in literature. NVOH yielded impressive rate performance and cycling stability, achieving 70.9 mA h g^{-1} at 1000 mA g^{-1} while retaining 78% of its discharge capacity after 150 cycles. This culminated with a full cell discharge capacity of 70 mA h g^{-1} when paired with C@V_2O_3 and an energy density of 100 W h kg^{-1} based on electrode mass. This represents a significant step forward in the development of electrode materials for both organic electrolyte SIBs and desalination.

Experimental methods

Materials synthesis

Commercial V_2O_5 (98%) and Na_2SO_4 (Reagent grade 99%) were purchased from ThermoScientific and used without further purification. Na_2SO_4 (aq, 0.28 mol dm^{-3}) was prepared in deionized (DI) water (>18 Mohm) and then 35 cm^3 aliquots were decanted into each acid digestion vessel (Teflon-lined, stainless steel jacket, 50 cm^3, Parr). Following this, 0.891 g of V_2O_5 was added to each solution, and the mixture was briefly stirred. The vessels were sealed and then heated at 180 °C for various durations (16–48 h). After leaving to cool, each product material was washed in sequential steps (using deionised (DI) water and centrifugation at 4000 rpm), until the conductivity of the supernatant was < 100 μS cm^{-1}. Following this, the solid products were vacuum dried at 70 °C overnight before use in electrochemical investigations. For the $V_2O_5 \cdot xH_2O$ sample, the hydrothermal reaction employed the same conditions for 16 h, but without the inclusion of Na_2SO_4.

For the scale up reaction larger hydrothermal vessels were employed and 80 cm^3 of 1 mol dm^{-3} of aqueous Na_2SO_4 were combined with 10 g and 25 g V_2O_3 precursor. They were heated to 180 °C for 24 hours with stirring, followed by identical washing and drying steps. In this process the 10 g sample was divided into two batches of identical colour, whereas the 25 g sample was divided into three batches with variation from red (batch 1, B1) to brown (batch 3, B3).

Physical characterisation

The synthesised powders were characterised by scanning electron microscopy (SEM, Apreo 2, Thermo Fisher Scientific), and by transmission electron microscopy (TEM, Talos F200i, Thermo Fisher Scientific, accelerating voltage 80 kV), including selected area electron diffraction (SAED). Powder X-ray diffraction, XRD, was also performed in the range $2\theta = 10–90°$ using a PANalytical X'Pert Pro diffractometer (UK), with Ni-filtered Cu Kα radiation (40 kV and 30 mA) and a PIXcel-1D detector. X-ray photoelectron spectroscopy (XPS, K-Alpha+, Thermo Fisher Scientific) was carried out to analyse the material surface, using monochromated AlKα radiation at 12 kV. Raman spectroscopy and Fourier transform infrared spectroscopy in attenuated total reflectance mode (FTIR-ATR) were undertaken using an InVia confocal microscope (Renishaw, UK, 532 nm laser from helium-neon source, 10% power) and a Spectrum Two Spectrometer (PerkinElmer, USA), respectively.

To analyse the bulk sodium-to-vanadium ratio, the powders were dissolved in *aqua regia* overnight (10 mg in 3 cm^3) of a 1 : 3 volume ratio of HNO_3 (68 mass%), and HCl (37 mass%) (both from Fisher Scientific, Trace Metal Analysis grade), followed by dilution and measurement. Quantitative analysis was performed using microwave plasma atomic emission spectroscopy (MP-AES, Agilent 4210). The concentrations of sodium and vanadium were measured using standards from 0.5 to 20 μg cm^{-3} prepared from commercial 1000 μg cm^{-3} stock solutions (PlasmaCAL) diluted with 2%vol HNO_3 (Trace Metal Analysis grade, Fisher Scientific). The emission signals of the analytes at 589 and 309 nm, for Na and V respectively, were normalised by ratioing by the intensity of beryllium, added as internal standard intensity (5 μg cm^{-3}, 234.86 and 313.04 nm) for correction of physical interfaces and sensitivity drift during analysis. The instrument was calibrated on a daily basis with freshly prepared standards, and the instrumental limits of detection (LOD, based on the $3 \times SD_{blank}$ criterion) were 0.3 μg cm^{-3} for both Na and V.

Electrochemical assemblies

Electrode materials were printed *via* the doctor blade method; first inks were made with an 80 : 10 : 10 mass ratio of active material, Super P carbon (Fisher) and PVDF (Pi-Kem, battery grade) which were dispersed in *n*-methyl-2-pyrrolidinone (NMP, Sigma-Aldrich) and mixed in a planetary mixer (Fritsch Pulverisette 7) for 10 min at 800 rpm. Inks were cast onto carbon foil using a variable applicator set to 150 μm, which had been briefly dried on a hotplate at 60 °C and then dried under vacuum for 24 h prior to entry into the glove box or use in aqueous cells, with a total mass loading of 1–1.5 mg cm^{-2}. Organic medium sodium ion batteries were assembled using 2032 coin cell casings, which included a glass fibre separator soaked in a solution of $NaPF_6$ (1 mol dm^{-3}) dissolved in diglyme, purchased premade, along with a sodium metal chip (all battery consumables purchased from Soion Tech). The batteries were assembled using a hydraulic crimping press (MTI) with a single stainless steel spacer (half cell) or two spacers (full cell).

Aqueous/desalination testing in 3-electrode cells used modified glass vessels with holes machined in the lids at fixed

distances, accommodating two 12 mm diameter graphite rod electrodes and a 7 mm diameter reference electrode. The working electrode was sheathed with electrical tape to restrict electrolyte access other than through the printed foil, which was secured to the rod by a silicone polymer jacket. The reference electrodes were homemade Ag/AgCl, made using potentiostatic anodisation. Briefly, silver wires (99.999%, Advent) were cut to 5 cm length, lightly sanded, and sonicated in deionized (DI) water, followed by placement in HCl (aq, 0.1 mol dm^{-3}) in a cell-electrode cell with commercial reference and graphite counter electrodes. Anodization was undertaken at 0.33 $V_{Ag/AgCl}$ until a 2.2 coulomb charge had been transferred.[26] For the housing of the electrode, a plastic 1 cm^3 pipette tip was selected; this tip had been placed in agarose gel (Invitrogen, Ultrapure, 7 g dissolved in 100 cm^{-3} at 50 °C, left to cool and solidify) to act as the frit, and was filled with NaCl(aq, 3 mol dm^{-3}) (NaCl from VWR, reagent grade).[27] Electrodes were screened prior to use, ensuring $\Delta V < |3|$ mV *vs.* a commercial Ag/AgCl reference and impedance < 1000 ohm. Each cell was tested using 50 cm^3 of NaCl (aq), and by both CV (1, 2, 3, 4, 5, 10 mV s^{-1}) and GCD (1000 cycles at 1000 mA g^{-1} from 1 to −1 $V_{Ag/AgCl}$).

Full organic medium cells were constructed using V_2O_3 embedded in carbon (C@V_2O_3), the synthesis, development and optimisation of which will be published in a separate work. Anodes were electrochemically sodiated prior to full cell assembly. This pre-sodiation used a 50 mA g^{-1} discharge current to a potential < 0.01 V *versus* Na/Na^+ in a 1.5 cm diameter Swagelok-style cell, using the same electrolyte and metal chips as the half-cells. Full cells were constructed using pre-sodiated anodes and NVOH cathodes, employing a coin cell architecture with an additional stainless-steel spacer and an identical electrolyte. Electrochemical testing was performed using Gamry reference 600 units (Cyclic Voltammetry, CV, and Electrochemical Impedance Spectroscopy, EIS), and galvanostatic charge–discharge (GCD) was performed using an Arbin BT2000 battery tester at low currents and a Landt CT3002A-5V1A instrument at higher galvanostatic currents.

Results and discussion

The synthetic procedure for NVOH production is summarised in Scheme 1, which involves the hydrothermal treatment of V_2O_5 powder in Na_2SO_4(aq) (0.28 mol dm^{-3}) for varying durations, followed by cleaning *via* centrifugation and drying in a vacuum oven. The sample VOH ($V_2O_5 \cdot xH_2O$), was synthesised by an analogous method using deionised (DI) alone, while the heat-treated sample NVOHT was produced by an additional 400 °C, 2-hour step after NVOH synthesis. The NVOH was first characterised by scanning electron microscopy to determine the powder morphology and its suitability for sodium storage applications. As widely reported,[13,18,28] the hydrothermal reaction yielded a high aspect ratio nanowire morphology, with structures visible after both 16 and 48 h of treatment (Fig. 1a and c, respectively). Although the varying duration of synthesis did not produce statistically significant differences in wires dimensions (as shown by the SEMs of all samples and statistical analysis, Fig. S1-3 and Table S1), a substantially larger number of distinct nanowires is visible after longer durations.

A closer view of the wires is seen in the transmission electron micrograph (TEM, Fig. 1c, including the selected area electron diffraction (SAED) inset) and a higher magnification SEM image (Fig. 1d), which shows distinct and separated wires. Such morphology appears highly favourable to ion transport due to a less tortuous ionic pathway through the wide volume between the wires (compared to a bulky grain morphology), and a greater surface area for the entry and exit of Na^+. Meanwhile, a high-magnification TEM image reveals lattice fringes (Fig. 1e) which appear to indicate a layered crystal structure for nanowires, with a wide spacing, 1.21 nm, corresponding to the labelled bright ring visible in the SAED. This evidence supports the data in Fig. 1f from X-ray powder diffraction (XRD), which determines the structure of NVOH, a critical factor in its suitability as an intercalation material.

The XRD patterns exhibit a uniform dominant phase for all synthesis durations, with strong peaks in the profile at 11.46, 23.97, 25.82, 28.58, 30.54, 39.71 and 50.78°. The reflections across all NVOH samples show a similar match to monoclinic NaV_3O_8 (mp-752972,[29] $P2_1/m$, used to index the peaks) but bear a systematic shift in several peaks, such as those indexed 100 and 110, to a lower angle. Meanwhile, the NVOHT sample shows far closer peak positions to the reference pattern; therefore, the treatment of 400 °C for 2 h caused a contraction evident in the XRD profile. For example, the 100 lattice spacing has been reduced from 0.772 to 0.686 nm from NVOH to NVOHT samples. The suggested cause is the removal of interlayer crystal water from the NaV_3O_8 lattice through heat treatment. The implications for sodium intercalation electrodes are mixed, with a high H_2O content being highly undesirable for long-term battery stability. In contrast, a wider interlayer distance can accommodate more sodium ions, resulting in greater capacity.

A sodium-poor, V^{4+}-rich impurity phase, NaV_6O_{13} (mp-780759) is detected, with XRD peaks labelled in the zoomed-in view and shrinking with duration of hydrothermal synthesis. This would likely hinder battery function as the phase would give low sodium mobility, through tunnels rather than interlayers, whilst costing the NVOH-phase capacity through lower sodium occupancy. The benefits, therefore, of increased hydrothermal duration are explained through the diagram in Fig. 1g, whereby after 16 h both NaV_3O_8 and NaV_6O_{13} are present through the sodiation of V_2O_5. However, this NVOH has a low sodium interlayer occupancy, which is then improved by further treatment as more of the $NaVO_3$ phase is converted into NVOH. The unit cell parameters of the 24 h sample was calculated through Pawley refinement as Monoclinic, space group *P* (1): $a = 7.775$ (3) Å, $b = 3.6003$ (6) Å, $c = 12.152$ (1) Å, $\beta = 95.44$ (1)°. Details for this calculation and the model fit can be found in the SI and Fig. S4, respectively.

Further details about the synthesised samples' surfaces were obtained from X-ray photoelectron spectroscopy (XPS), which revealed the elemental composition, chemical environment, and ionisation states of the species present (Fig. 2a–e). A survey scan of the 48-hour NVOH sample (Fig. 2a) shows the presence of carbon, oxygen, vanadium, and sodium, with ratios of Na : V :

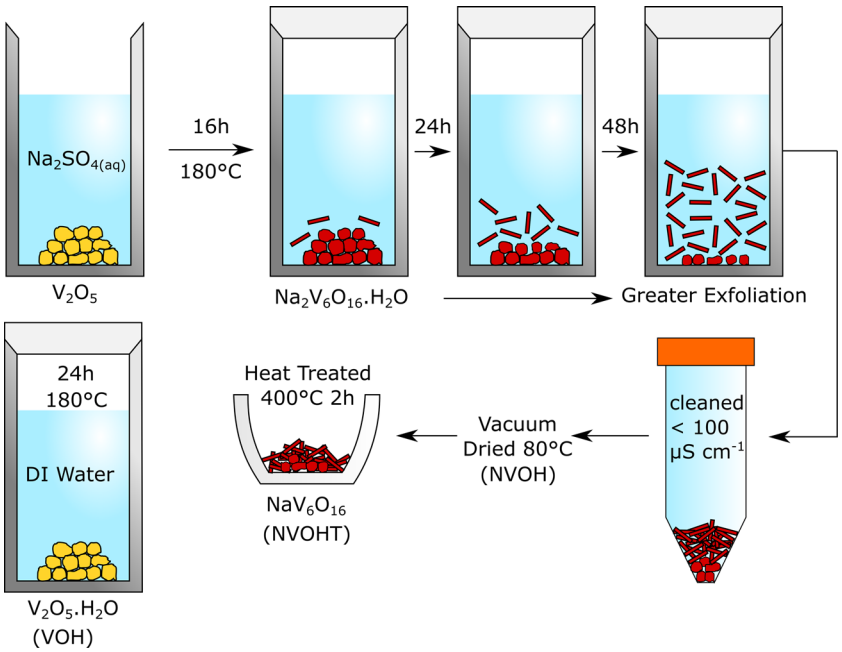

Scheme 1 Shows the synthetic protocol for the hydrothermal synthesis of NVOH from precursor V_2O_5 using pressurised acid digestion vessels with stainless steel jackets and PTFE liners. Longer durations are predicted to produce greater exfoliation of nanowire morphology. Synthesised powders were washed with water and centrifugation until the supernatant conductivity was below a threshold. Following vacuum drying at 80 °C, the powder was collected as NVOH. Additional heat treatment produced NVOHT, and hydrothermal treatment of V_2O_5 with deionised (DI) water was used to make VOH.

O close in value to those of the XRD reference (1.77 : 6 : 16.4; all survey scans are shown in Fig. S5). The V 2p high-resolution scan, shown in Fig. 2b, compares the sodiated samples with the precursor V_2O_5, with an expected spin–orbit coupling ΔE of 7.4 eV (1 eV = 1.6×10^{-19} J) for the $2p_{3/2}$ *vs.* $2p_{1/2}$ states. The samples primarily exhibit V^{5+} and a small addition of V^{4+}, comparable to the precursor V_2O_5 surface. The V^{4+} has nearly disappeared in the 48-hour sample, likely due to full sodiation/oxidation from NaV_6O_{15} to $Na_2V_6O_{16}$. The oxygen 1s and carbon 1s scans (Fig. 2c and d, respectively) both show an initial high proportion of adventitious carbon species, including C–O and C═O groups, after 16 h. In both cases, however, the intensity of these signals decreases monotonically with duration, leaving the metal oxide (M–O) peak to dominate the spectrum. The quantity of surface carbon substantially decreases with heat treatment duration, as shown in Fig. S6.

The powders were further characterised by Raman and Fourier Transform Infrared (FTIR) spectroscopies (Fig. 2f and g) to confirm the proposed structures. The precursor, α-V_2O_5, consists of chains lying along the *y*-axis (Fig. 1g), with each vanadium atom forming four polar V–O bonds. The four bonds are assigned to the following peaks: V═O1 at 993, V–O3 in a V–O–V bridge at 526, and two V–O2 bonds at 696 cm^{-1}, oriented along the chain, linking them together in a ladder.[32] Other phonon excitations, such as oscillations perpendicular to the chain in ladder mode, explain further peaks, including those at 143, 282, and 302 cm^{-1}. Those phonon peaks are present for all samples, confirming the expected chains of octahedral vanadium. Peaks at 480 and 526 cm^{-1}, on the other hand, are intense for the V_2O_5 precursor but are significantly reduced in all sodiated samples. These two peaks are assigned to the ladder step stretching vibration and symmetric stretching ν_s(V–O3–V) modes, respectively; their decrease is likely due to the great restriction placed on each V octahedron, locked in place by its four neighbours in the NVOH layer structure. The FTIR spectra, meanwhile, confirm the presence of V–O–V and V═O bonds in all samples, but also show additional sharp peaks at 1635 and 3585 cm^{-1}, indicating the presence of crystal water in the interlayer structure.[33]

The presence of crystal water was confirmed by thermogravimetry (TG) with differential scanning calorimetry run in flowing nitrogen, which showed three plateaus (Fig. 2h), for all samples, indicating mass loss events. Initial mass losses from ambient to 120 °C are attributed to the evaporation of surface water from the powders, culminating in a peak in the differential heat flow in the 16-hour sample at 120 °C, which is observed in all samples (Fig. S7). A steady mass loss gradient persists up to 350 °C, which is attributed to the loss of interlayer crystal water, as quantified by subtracting the total loss from the initial surface evaporation.[17] A full quantitative comparison of water content, *n*, is shown in Fig. 2i for $Na_xV_3O_8 \cdot nH_2O$, where the sodium content was determined by microwave plasma atomic emission spectroscopy (MP-AES) after dissolving the powders in aqua regia. A monotonic increase in interlayer (crystal) H_2O content with synthesis duration is observed, indicating further hydration of the interlayer Na^+ ions.

Regarding the bulk Na content (determined by MP-AES) compared to V_3, the 16-hour sample showed low sodiation at

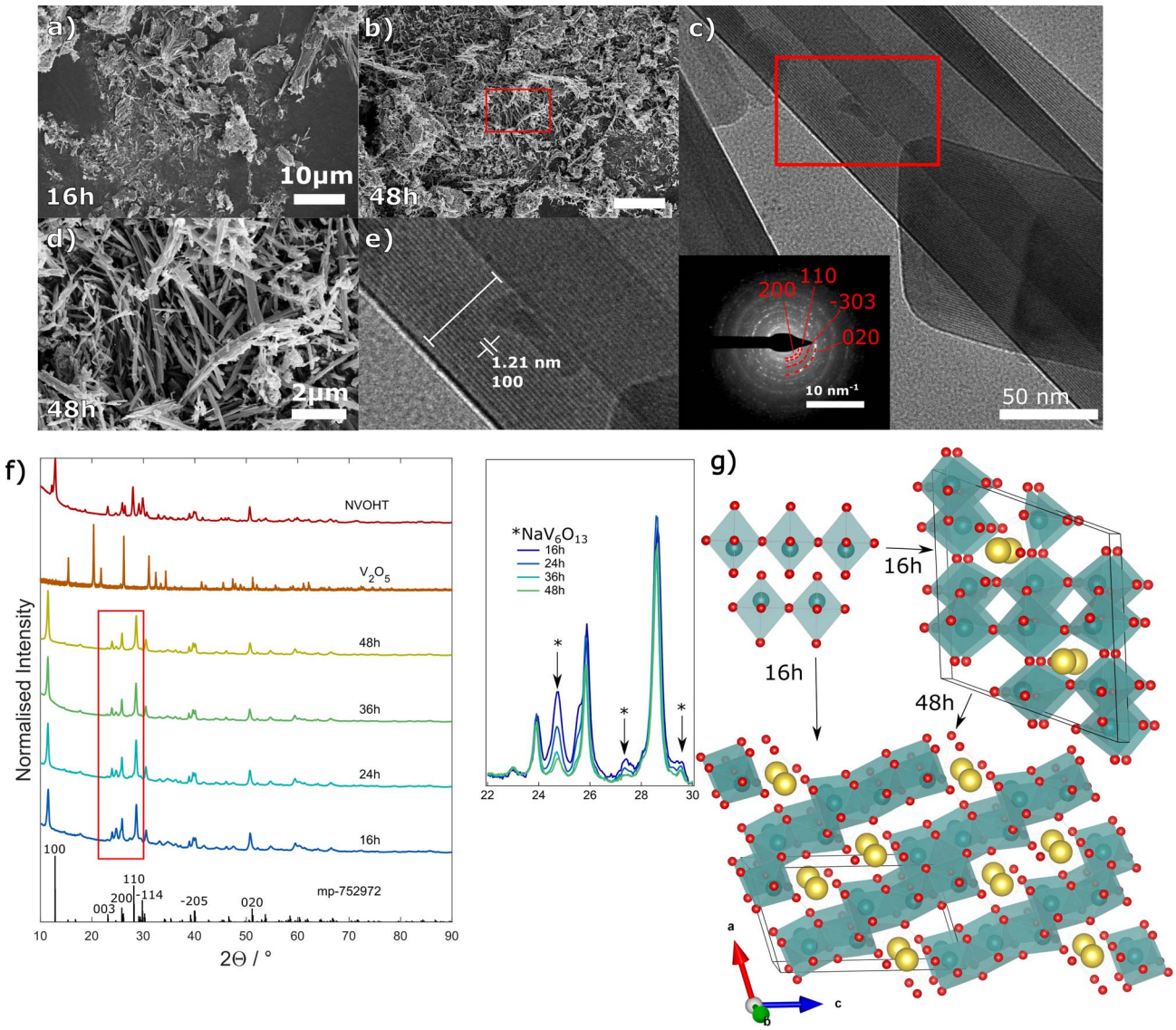

Fig. 1 (a) Shows the SEM image at low magnification hours of NVOH nanowires produced after 16 h, while (b) shows the 48-hour sample at the same magnification. Nanowire morphology of the 48-hour sample is shown in greater detail from low magnification TEM with SAED inset, (c), and high magnification SEM (d). (e) Shows a high-magnification TEM with lattice fringes; the spacing was measured from a survey of 10 peaks. Powder XRD profiles are shown in (f), including the indexed $Na_2V_6O_{16}\cdot 3H_2O$ pattern,[30,31] V_2O_5 after 16 h at 180 °C in DI water, and NaV_6O_{15}, which resulted from post-heat treatment of the 24 h sample. Crystal structures show the evolution of phases through longer hydrothermal duration (g).

$Na_{0.85}V_3O_8$, which increased to a plateau of $Na_{1.1}V_3O_8$ for 24, 36, and 48 h. The surface Na measured by XPS showed a great similarity to the bulk content of the 16-hour sample but remained at around 0.8 at the surface. This is likely due to the presence of the sodium-poor NaV_6O_{13} indicated by XRD, whilst the noticeable decline in surface V^{4+} observed with longer durations of hydrothermal reaction follows the previous trend in decrease of this phase. In summary, the structure of $Na_xV_3O_8\cdot nH_2O$ was confirmed, with full sodiation occurring after 24 h. Meanwhile, the content of the low-sodium phase NaV_6O_{13} is reduced, and the interlayer H_2O content increases monotonically with reaction duration. The values of bulk compositions yielded for 16, 24, 36 and 48 h were $Na_{0.85}V_3O_8\cdot 0.51H_2O$; $Na_{1.14}V_3O_8\cdot 0.72H_2O$; $Na_{1.05}V_3O_8\cdot 0.86H_2O$; $Na_{1.14}V_3O_8\cdot 1.3H_2O$, respectively.

A sodium ion cathode for use in organic media

To determine the charge storage characteristics of the NVOH samples, they were tested in sodium ion half-cells against sodium metal counter electrodes, as shown in Fig. 3. Fig. 3a shows the cyclic voltammetry (CV) for electrodes made with the 24-hour sample and at scan rates ranging from 1 to 10 mV s^{-1}. Two key features emerge from the oxidative wave: peaks A and B are attributed to two oxidation events and were visible in all samples (Fig. S8), with little polarization at faster rates. The corresponding reductions are assigned to C and D for B and A,

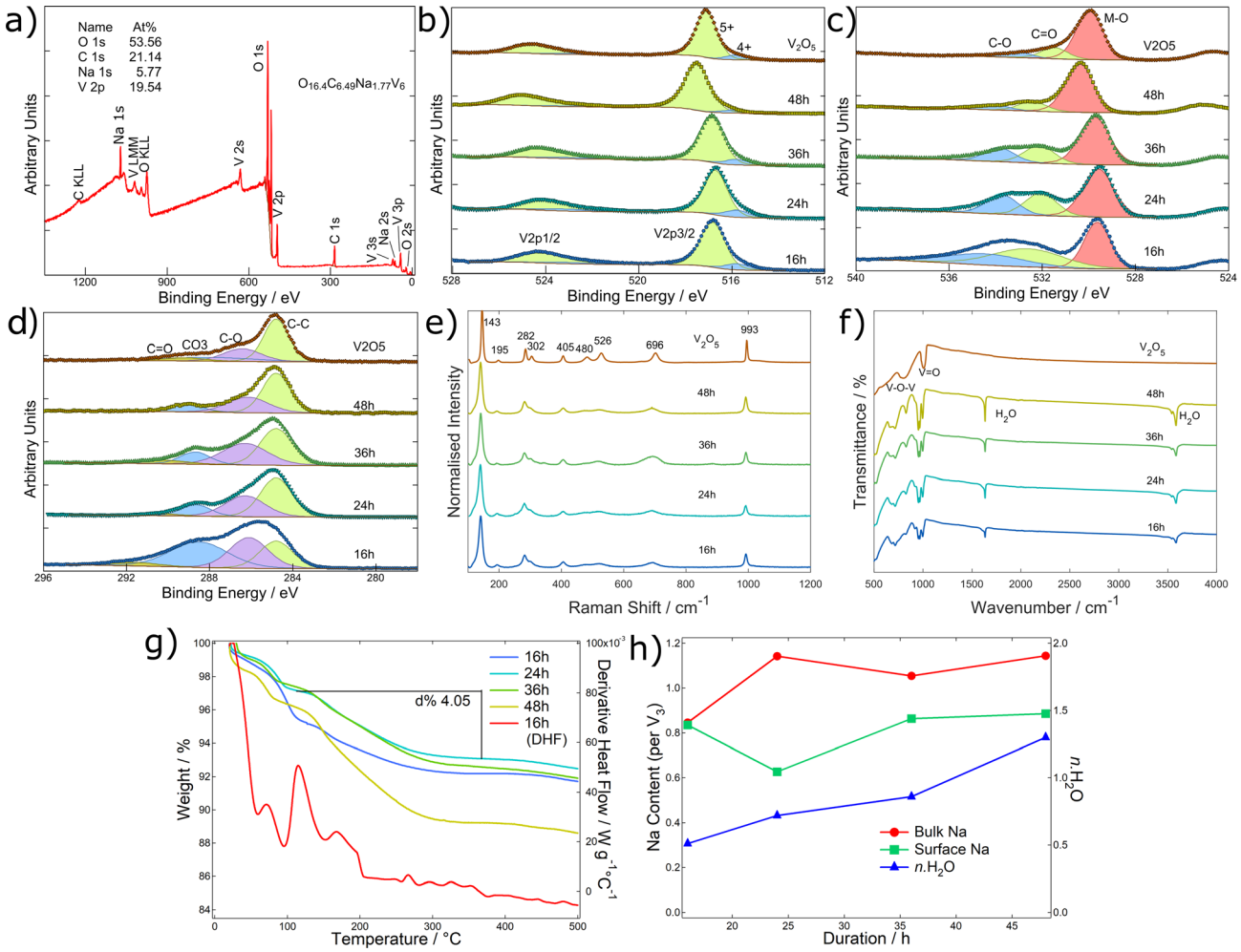

Fig. 2 Shows XPS data for the various synthesis durations, including a survey scan for the 48-hour synthesis, (a), carbon 1s scan for precursor V_2O_5, and all synthesised samples in (b), oxygen 1s scan in (c) and finally vanadium 2p scan in (d). Raman and FTIR spectroscopies of the samples are presented in (e and f), respectively. Finally, the TG and derivative heat flow of the 16-hour sample are shown in (g), and the atomic ratio of Na to V_3, as measured by dissolution MP-AES (bulk) and XPS (surface), is compared with the presence of crystalline water (h).

respectively. Full CV traces were used to calculate the charge storage capacity (Fig. 3b) and the Trasatti method was used to calculate the ratio of diffusive charge to surface charge (Fig. 3c), with calculations detailed in the SI. From these data, it is clear that the majority of the charge storage capacity, as measured by CV, arises on the surface as pseudocapacitive storage, likely due to the high surface area morphology.

Little difference in the ratio of diffusive to surface charging was observed from the NVOH samples (Fig. S8) but substantial differences were detected for the VOH and NVOHT samples, Fig. S9. The VOH showed over double the diffusive charge percentage at 10 mV s^{-1} (26.2%) compared to the NVOH samples (11.2%), which increased further for the NVOHT sample to 36.2%. This is due to the favourable morphology of NVOH over VOH; channels between NVOH nanobelts provide ionic pathways into the electrode. Meanwhile, the wide interlayer spacing in the nanowire structure likely increased the pseudocapacitive charge for the NVOH over NVOHT. The 24-hour sample showed peaks with the highest current density per unit mass loading and, therefore, the highest capacity across all scan rates.

To understand the effects of sodiation and H_2O content on sodium diffusion through the bulk, the Randles–Sevcik equation was used to determine the diffusion coefficient at various rates. Initially, peak current i_p (A) for peaks, A and D were plotted against the square root of the scan rate v (V s^{-1}), showing linear relationships, Fig. 3d. The diffusion coefficient D (cm^2 s^{-1}) was then calculated from the gradient of the fit, using the number of electrons exchanged (n,1), the area of the electrode A and the concentration of the electrolyte C.

$$i_p = 2.686 \times 10^5 n^{3/2} A D^{1/2} C v^{1/2}$$

The resulting curves show a similar trend for desodiation (peak A) and sodiation (peak D), whereby the diffusion coefficient decreases with a greater duration of hydrothermal synthesis, as shown in Fig. 3d and e. This is likely due to a greater population of Na^+ and H_2O saturating the interlayer,

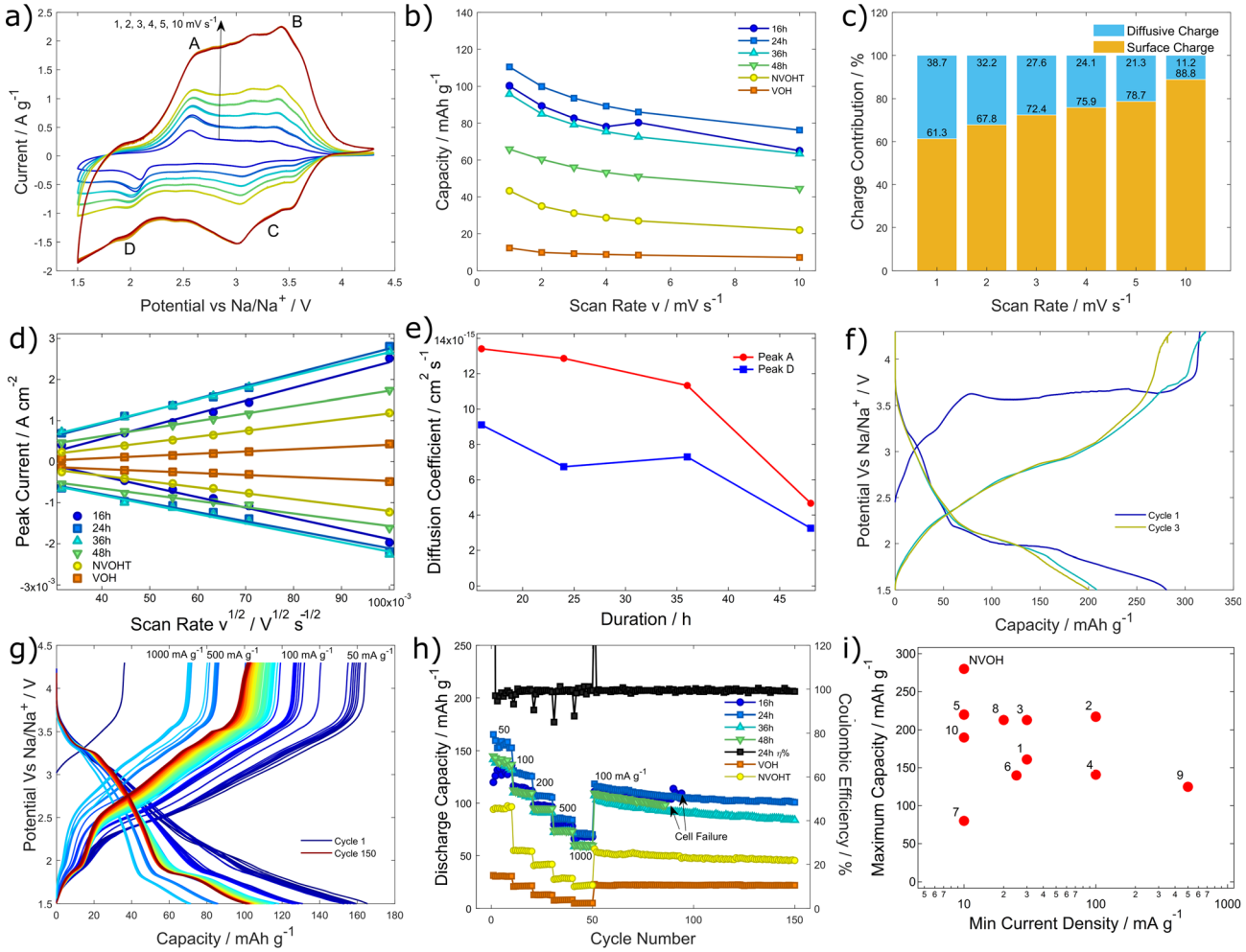

Fig. 3 Shows the electrochemical performance of the NVOH electrodes using various techniques, (a) shows the CV traces with the 24-hour sample at various scan rates, (b) shows the integral capacity measured from the CV trace *versus* scan rate, and (c) shows the result of the Trasatti calculation for the 24-hour sample, showing the surface *versus* the diffusive charge ratios at different rates. The peak current plotted against the square root of the scan rate is shown in (d), while the diffusion coefficient, as calculated by the R–S equation, is displayed in (e). Slow charge rate GCD (10 mA g^{-1}) for the first 3 cycles is shown for the 24-hour sample in (f), with varying rates in (g). The rate capability and stability of the samples, as well as the coulombic efficiency with the 24-hour sample, are shown in (h). A comparison to the published capacity maximum of NVO applied to sodium-ion half-cells is shown in (i), corresponding to the following references (symbol [reference]) 1 (ref. 15), 2 (ref. 16), 3 (ref. 34), 4 (ref. 12), 5 (ref. 14), 6 (ref. 35), 7 (ref. 10), 8 (ref. 36), 9 (ref. 11), 10 (ref. 8).

crowding the diffusion pathways. Conversely, all samples showed substantially higher diffusion coefficients than the VOH (4.1×10^{-16} and 3.2×10^{-16} cm^2 s^{-1} for peak B and D respectively) and the NVOHT samples (2.8×10^{-15} and 2.9×10^{-15} cm^2 s^{-1}) due to their larger inter-layer spacing, as inferred from XRD data. This trend was confirmed using galvanostatic intermittent titration technique (GITT, described in SI) using 50 mA g^{-1} pulses for 5 minutes followed by 30 minutes of relaxation time, Fig. S10. The NVOH sample (36 h) showed a peak diffusion coefficient at 9.5×10^{-14} cm^2 s^{-1} and a plateau at 1.9×10^{-14} cm^2 s^{-1} during charging, whereas the VOH sample and NVOHT sample showed plateau averages at 4.1×10^{-15} and 1.1×10^{-15} cm^2 s^{-1}.

The 24-hour sample showed an impressive initial capacity of 280.1 mA h g^{-1}, as measured by galvanostatic charge–discharge, GCD (Fig. 3d, initial three cycles tested at 10 mA g^{-1}). This value was significantly higher than those of the other durations: 165.1, 143.9, and 157.5 mA h g^{-1} for NVOH samples prepared after 16, 36, and 48 h, respectively (Fig. S11). Upon repeating measurements with three separate coin cells, the 24-hour duration showed an average first-cycle capacity of 233.0 ± 57 mA h g^{-1}, which is significantly higher than the other samples. The intercalation reaction of the NVOH during discharge is largely absent in the SIB literature, however, it is proposed that it follows the following half-cell reaction:

$$NaV_3O_8 + xe^- + xNa^+ \leftrightarrow Na_{1+x}V_3O_8$$

This allows for the calculation of sodium content and vanadium oxidation using the specific capacity, as shown in the SI (Fig. S11), which for 280.1 mA h g^{-1} yields an expected

additional sodium of $x = 3.2$ and an oxidation state of V^{3+}.[9] Further *in operando* studies are needed to confirm this mechanism.

The rate capability was further tested, yielding values of 165.4, 130.9, 107.8, 85.5, and 71.5 mA h g^{-1} at 50, 100, 200, 500, and 1000 mA g^{-1}, respectively (Fig. 3e and f), followed by 100 cycles at 100 mA h g^{-1}. At a high cycle number, the electrode continues to exhibit dual redox events, as evidenced by the presence of dual plateaus in the rainbow plot. The performance was similar for the various durations. However, the 16-hour material led to the lowest capacity, 50 mA g^{-1}, the low value likely due to reduced sodiation. The 24 and 36-hour samples led to the best stability, achieving 100.8 and 83.8 mA h g^{-1} at cycle 150, respectively. NVOH from the other synthesis durations led to early device failure, likely due to the presence of unstable $NaVO_3$ in the 16-hour sample and high water content in the 48-hour sample.

Unsurprisingly, cells containing the NVOH samples greatly outperformed the VOH and NVOHT samples at all rates (10 mA g^{-1}, Fig. S11), experiencing a particularly severe reduction in specific capacity from current densities 50 to 1000 mA g^{-1}. This is due to the significantly reduced diffusion coefficients measured by CV; the reversible intercalation of Na^+ is stifled at high currents. Critically, the presence of interlayer water and high sodiation level following use of 24-hour NVOH synthesis allow far greater rate capability.

In comparison to the literature shown in Fig. 3g, the 24-hour maximum capacity achieved in this study, 10 mA g^{-1}, was significantly higher than the capacity maxima reported in the previous studies (selecting for Na-ion half cells, Table S2). This is believed to be due to the optimised sodiation, as well as critically controlled quantities of crystal water which ensures wide interlayer spacing for high-volume sodium ion storage. For the publications observed, all samples, other than polypyrrole coated NVO, underwent thermal treatment > 250 °C prior to cell testing, removing this crystal water.[34] However, this may also be due to several studies testing at high current densities as their minimum charge rate. Additional interlayer water may also give rise to dissociated protons participating in the redox chemistry, which explains the low initial cycle coulombic efficiency and the drop from 280 to 200 mA h g^{-1} in subsequent cycles.

Sodium ion half cells were cycled further (Fig. S12a), up to 500 cycles at 100 mA g^{-1}, for comparison of long-term stability, where the 24 h and 36 h samples survived to ~450 and 250 cycles, respectively, before failure. Although the NVOHT and VOH cells remained functional at 500 cycles, this represented a fraction of the time duration. In the case of NVOHT it degraded more rapidly to 36% of its initial capacity, compared to the 24 h sample at its failure point retaining 67% of its initial capacity. This further shows the improvement to stability the structural water provides to the oxide.

In comparison to previous literature, the 24-hour sample gives improved cell stability and rate capability. For example, in the work by Yuan *et al.*, a capacity of 75 mA h g^{-1} at 500 mA g^{-1} was reported, compared to 85.5 mA h g^{-1} in this work. Additionally, 100 mA h g^{-1} was retained after 50 cycles, compared to 100.8 mA h g^{-1} after 150 cycles, as reported here.[8] This also represents a step up, relative to Ca- and F-doped NVO, as reported by Han *et al.*, who achieved 65.8 mA h g^{-1} at a 400 mA g^{-1}, rising to 104.9 mA h g^{-1} after 100 cycles.[14] Rather than any additional dopants, interlayer water incorporated during synthesis can itself stabilise interlayer reversible sodium extraction, improving rate capability and maximum capacity relative to NVO with additional dopants.

In comparison to other sodium ion cathode materials, the NVOH performs competitively with the highest capacity state-of-the-art materials. Prussian blue analogues present a widely explored family of materials with the composition $Na_xM_1[M_2(CN)_6]_y \cdot zH_2O$ where M_1 and M_2 are transition metal ions, with dual electron specific capacity of 150 mA h g^{-1}.[37] Single electron transfer materials such as those that use Ni show excellent long term stability (88% at 10 000 cycles at 10C) at a lower initial specific capacity of 66.8 mA h g^{-1}.[38] One Fe based, dual electron candidate, Prussian White, presents a promising commercial sodium ion cathode, showing a specific capacity of 167 mA h g^{-1} at 0.1C and reasonable performance at −25 °C, though questions remain over cycling stability.[39]

Meanwhile, NASICON (Na Super Ionic Conductors) structured $Na_3V_2(PO_4)_3$ shows reasonable charge capacity (130 mA h g^{-1}) as well as an impressive rate capability of 76.2 mA h g^{-1} at 40 °C.[40,41] Greater charge is also possible with heterogeneous forms of the material: $Na_4Fe_3(PO_4)_2(P_2O_7)$/$Na_2VTi(PO_4)_3$ synthesised by Zu *et al.*, achieved charge storage of 155 mA h g^{-1}.[42] Finally, metal oxides show some of the highest sodium storage capacities in literature, particularly those with O3 layered type crystal structures, such as $NaNi_{1/2}Mn_{1/2}O_2$ with a 15 mA g^{-1} capacity of 200 mA h g^{-1}.[43] Due to dramatic phase changes seen during desodiation, these materials suffer from rapid degradation on a 50 cycle scale, which can be mitigated by Ti and Mg doping. This work shows that the NVOH outperforms many of these materials, whilst requiring a simpler one-step synthesis with two primary reagents. This speaks to the industrial relevance of the material and potential for scalability.

In order to demonstrate this further the material was synthesised on a 10 and 25 g scale, with results shown in Fig. S12, where the 10 g sample showed homogenous red colour across division into two batches, while the 25 g sample was inhomogenous across batches: one was red and other two were more yellow/brown. This is reflected in the powder XRD, where the 10 g sample showed identical phase formation to the 1 g across both batches, but the 25 g sample batch 3 showed peaks corresponding to VOH instead. Furthermore, identical rate capability tests were performed on the printed scale up powder and repeated in 1 M $NaPF_6$ diglyme half cells, showing high reproducibility and comparable performance to the 24 h sample for the 10 g sample. Though the capacity was significantly lower at higher rates this is likely due to unoptimized morphology which would need to be investigated further. The 25 g sample on the other hand showed a poorer performance, likely due to reaching the limit of the vessel size, causing insufficient sodiation and water intercalation: this is unsurprising as it was twice the vessel volume for 25 times the initial precursor mass. This initial work confirms that the NVOH is not only highly competitive when it comes to cell performance, but the batch

hydrothermal synthesis method is scalable for future commercial production of sodium ion batteries.

This study of NVOH was then advanced further towards real-world application in organic media, by testing in a full device against a carbon-coated V_2O_3 anode, C@V_2O_3, that had been developed in tandem with this study and which will be detailed elsewhere. The CV traces for half cells at 1 mV s^{-1} with the individual cathode materials, Fig. 1a, show their compatibility for a full device, whilst CV traces of the completed full cells with mass ratios of 1 : 1.8, 1 : 1.9, 1 : 1.5, 1 : 1.1 of anode:cathode coating indicate oxidation beyond 4 V, and the beginning of further redox activity at 1 V, Fig. 1b. Therefore, a voltage window of 0–4 V was selected for these devices in GCD testing at 100 mA g^{-1}, indicating reasonable stability and good coulombic efficiency across the first 100 cycles for the 1 : 1.9 cell (Fig. 4c and d). This reflected a high discharge capacity of 69.8 mA h g^{-1}, calculated using the total active material mass in the anode and cathode, and a 98% capacity retention over this period. A greater capacity was observed in the 1 : 1.1 cell, reaching 78.4 mA h g^{-1}, but after 100 cycles that declined to 69% of its initial performance. This decline is likely due to the higher voltage compared to Na/Na^+, at which the comparatively low mass cathode would be driven during charge, potentially causing continued oxidation of the electrolyte and leading to a build-up of degradation products.

Meanwhile, these devices reflected a maximum mass-energy density of 96.7 and 104.0 W h kg^{-1} for the 1 : 1.9 and 1 : 1.1 devices, respectively. Two other ratios were tested but resulted in poor performance, likely due to damage during the disassembly and handling of the anodes sustained in the pre-sodiation step required due to the low sodiation level of the cathode (in comparison to lithiation of a LIB cathode). This issue is common with SIB cathodes and presents a significant challenge to overcome in future work. Finally, the EIS (electrochemical impedance spectroscopy) plots show low charge transfer resistances for all samples, particularly in the 1 : 1.1 device, where dual arcs are visible, those likely to result from the anode and cathode, as shown in Fig. 4g.

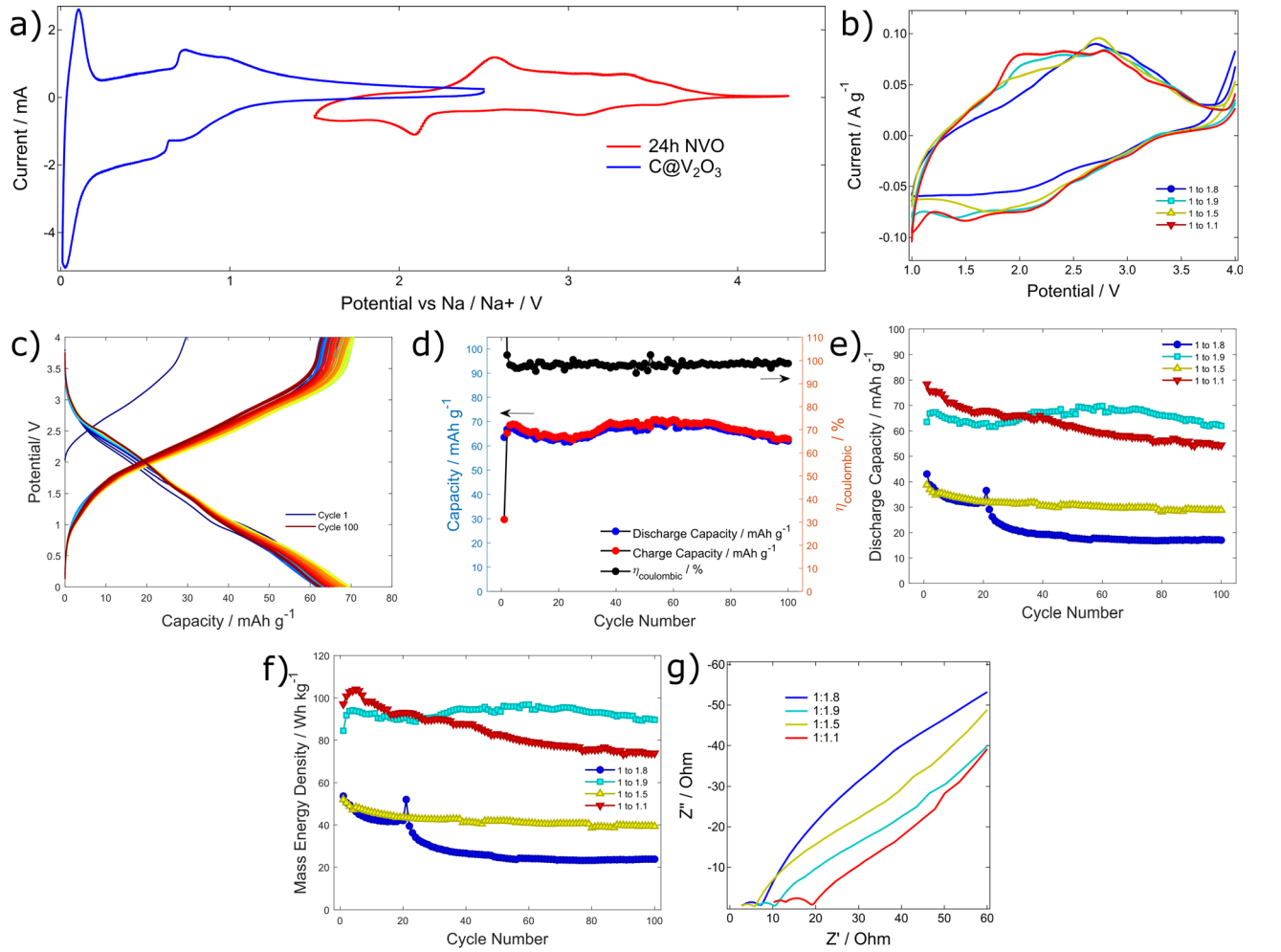

Fig. 4 Shows the electrochemistry of the organic medium full cell, OFC, with an initial half-cell CV trace and cathode and anode measured at 1 mV s^{-1}, (a) and 2-electrode CV traces for full cells with various mass ratios of the anode to cathode coatings, (b). (c–e) show the cycling performance of the various full cells tested by GCD. (f) Shows the mass-energy density for the full cells, as calculated from the total mass of active cathode and anode materials. (g) Shows the precycle EIS (electrochemical impedance spectroscopy) data for the devices.

These values of full cell specific capacity (calculated using the sum of the active masses of anode and cathode) represent a key step forward in the development of SIBs towards real-world applications, as they surpass the current state of the art in the literature for NVO-type materials. Critically, the Ca- and F-doped full cell constructed by Han *et al.* showed a maximum capacity of *ca.* 60 mA h g^{-1}, which declined to less than 40 mA h g^{-1} after 100 cycles.[44] Various other studies have calculated higher values than this but seemingly take into account the mass of the NVO (or composite NVO) as cathode or anode material. An adjusted calculation based solely on NVOH mass is presented in the SI, which reveals the highest full cell capacity reported in the literature (see full literature comparison in Table S1).

Aqueous sodium-ion storage for desalination

In order to confirm the effective sodium ion storage properties of the NVOH electrode for desalination applications, a methodology was developed using a high-volume cell (50 cm^3 NaCl (aq) 3 mol dm^{-3}), a sheathed graphite rod current collector, an unsheathed graphite counter electrode, and a homemade Ag/AgCl reference electrode, Fig. 5a and b. The exposed graphite rod was able to absorb the electrolyte, yielding a high surface area solution contact, and therefore, provided a strong capacitive response in CV traces (Fig. S14a), with strong tails of water oxidation and reduction. The sheathed graphite, meanwhile, showed a significantly reduced response, implying restricted electrolyte access to the pore volume by the carbon foil, which confirms its suitability as the working electrode compared to the high exposed surface area, unsheathed counter electrode. The utility of the system for testing printed electrodes was confirmed by substantial increases in both the areal current and charge capacity relative to the carbon foil alone, calculated form the full integral of CV traces, as shown in Fig. S14b and c. Specific current densities were estimated using the active material mass of the print, with the 36-hour sample at various scan rates and over the voltage range −1.2 to 1.2 $V_{Ag/AgCl}$ (Fig. 5c).

Peaks analogous to those in half-cell CV traces are visible on a backdrop of solvent breakdown at higher rates. The various NVOH samples are compared in Fig. 5d and e, where the 24-hour and 3-hour samples show the greatest enclosed area in traces at 10 mV s^{-1}, indicating the greatest charge storage. The charge capacity calculated from the full area of the CV traces once again showed that 24-h material gave significantly greater capacity at scan rates of 1–5 mV s^{-1}, due to optimised sodium and crystal water content. At 10 mV s^{-1}, the 36-hour sample gave the highest performance, likely due to lower NaV_6O_{15} content. The values themselves were significantly higher than those obtained by CV in organic media, due to more complex charge mechanisms and including a contribution from the carbon foil and electrolysis, but true charge capacity cannot be determined in a 3-electrode CV system. This is made clear by the similar surface *versus* diffusion-limited charge storage calculation for the 36-h electrode, Fig. S14d. At 10 mV s^{-1}, the diffusion-limited charge contribution increased from 13.1% (organic) to 66.9% (aqueous), most likely due to mass transport associated with electrolysis. Despite this, the cells with locally made, reference electrodes offer a low-cost, high-throughput platform for exploring future electrode materials and electrolytes for aqueous application.

The systems were further tested *via* GCD cycling, with narrowed potential limits of 1 to −1 $V_{Ag/AgCl}$, typical of electrochemical desalination; 2-electrode systems often discharge and charge to negative and positive potentials, Fig. 5f. In several examples in the literature, the discharge capacity is calculated from maximum voltage (1 V) to minimum voltage (−1 V) despite like signs for negative current and voltage indicating that, in 2-electrodes mode, a charge process is occurring, requiring energy input.[21,23,24] That would mean that electrolysis occurring during energy input would have been included in a discharge capacity. In this work, however, the discharge capacity is calculated as shown in Fig. 5h, from absolute maximum voltage to 0 V, as either an 'up' cycle or a 'down' cycle, defined by whether the charge voltage extreme is positive or negative, respectively. The use of 0 $V_{Ag/AgCl}$ as the maximum point of discharge is justified because Ag has been used as a chloride storage electrode for desalination batteries.[23,45] By this means in this study, a realistic recoverable specific capacity can be obtained for the material based on Na^+ storage in a saline (NaCl(aq)) system.

The voltage/capacity plot for the 24-h sample is shown in Fig. 5g, indicating a low recovery of charge 32–21% when calculating coulombic efficiency from discharge −1 to 0 $V_{Ag/AgCl}$, divided by charge from 0 to −1 $V_{Ag/AgCl}$, due to a large resistive overpotential. This is contrasted with calculating coulombic efficiency calculated from the full −1 to 1 $V_{Ag/AgCl}$, giving 105%, Fig. S15, showing that losses due to uneven electrolysis (more moles hydrogen evolved than chlorine) are minimal. The resultant cycling capacities are displayed in Fig. 5h, where far greater sodium storage occurs during the 'down' cycle, when NVOH acts as an aqueous battery anode. The 24-h material once again outperforms all others in stability, retaining a specific capacity of 25.3 mA h g^{-1} at 1000 mA g^{-1} at cycle 1000. This is after a peak capacity of 81.5 mA h g^{-1} at cycle 24, reflecting additional sodium intercalation x of 0.9 and an oxidation state of V^{+4},[7] Fig. S13.

This promising stability and capacity could yield an ideal electrode for sodium ion storage, particularly for desalination, which involves generating fresh water from seawater or from brine concentrates discharged from reverse osmosis desalination plants. The implementation of electrochemical desalination could utilize this concentrate to store electrical energy as a battery or for further desalination during charging. To evaluate the effectiveness of a desalination cell with sodium storage in NVOH, the cell was tested in a typical GCD mode (1000 mA g^{-1}) with 5 drops of universal indicator to observe any localised changes in pH, and was filmed using time-lapse (SI Video S1). Video frames at key potentials were extracted to understand these processes, as shown in Fig. 6a–d. The figure reveals no pH changes at positive potentials but the clear generation of acidic (giving red colouration) and basic (giving

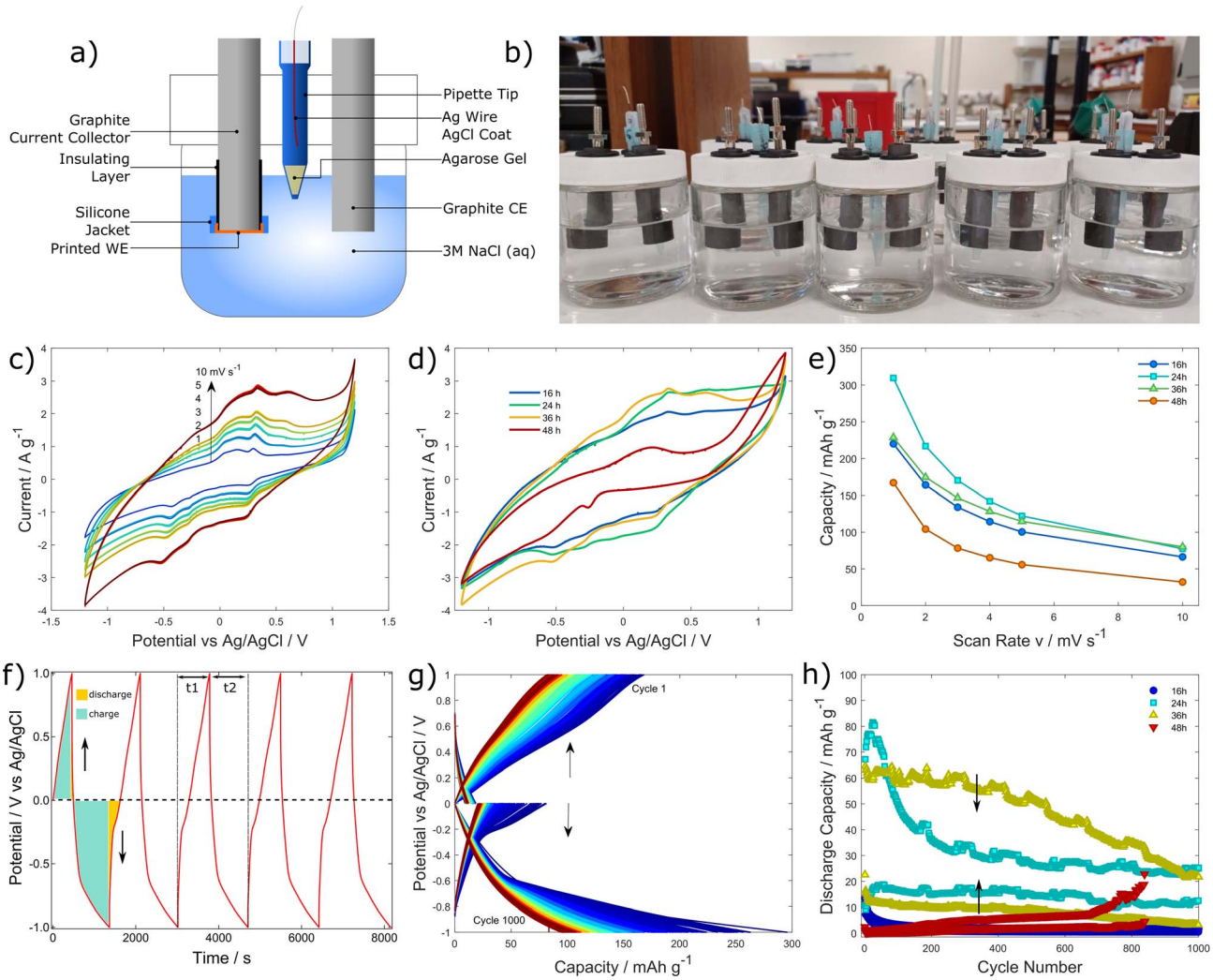

Fig. 5 Shows a schematic and photograph of the aqueous testing cell used for testing the NVOH electrodes in NaCl(aq), for application in desalination, (a and b). The resultant CV traces of the sample at various scan rates are shown in (c), and comparison at 10 mV s^{-1} of all the durations is presented in (d). Capacities determined from the CV traces as a function of scan rate are shown in (e). For GCD cycling, the voltage program used is displayed in (f), including details of charge/discharge regions of the cycling. The voltage–capacity plot for the cycling is shown in (g) for the 24-h sample and in (h) for the variation in capacity for the various electrodes during cycling at 1000 mA g^{-1}.

blue colouration) species at the counter electrode (left) and at the working electrode (right) at negative potentials.

This is most likely due to a modified chloralkaline process where typically Cl_2(g) is generated through brine electrolysis, along with NaOH(aq) at the counter electrode. The key difference is that sodium storage by intercalation into the NVOH material prevents rapid disproportional generation of OH–, as observed in opposing pH changes, and only small changes in the electrolyte pH over a 1000-cycle period (pH change from 6 to 8). What is observed on counter-cycling is the delamination and release of material at positive potentials, which accounts for the decline from the capacity peak in Fig. 5h; post-measurement weighing revealed a mass loss of 0.1 mg. This delamination represents a critical issue that needs to be addressed in future work.

In order to take advantage of the voltage accuracy of the three-electrode system, *in operando* potentiostatic EIS (from 1 MHz to 0.1 Hz) was performed using the 24-h sample, extracting effective series resistance, ESR, using the linear intercept of the high-frequency data points with the real, Z', axis, Fig. 6e. The EIS measurements were taken at sequential values of DC voltage (the AC maximum was maintained at 10 mV), incremented by 0.2 V each time. The Bode plots in Fig. 6f show two key negative peaks, indicating two significant resonant effects corresponding to two distinct timescales. The peak occurring at around 100 Hz can be assigned to the timescale of electrolysis due to its overlapping prevalence at −1 and 1 $V_{Ag/AgCl}$, whereas the peak occurring at around 1 Hz could be due to sodium intercalation effects, corresponding to the redox features observed in the CV traces. Both occurrences on relatively long timescales imply a mass transfer/diffusion-limited event. The voltage extrema are reflected by distinct arcs seen in the Nyquist 3D plot attributed to electrolysis. This is reflected in peaks observed in the diffusion coefficient and capacitance plotted with DC voltage,

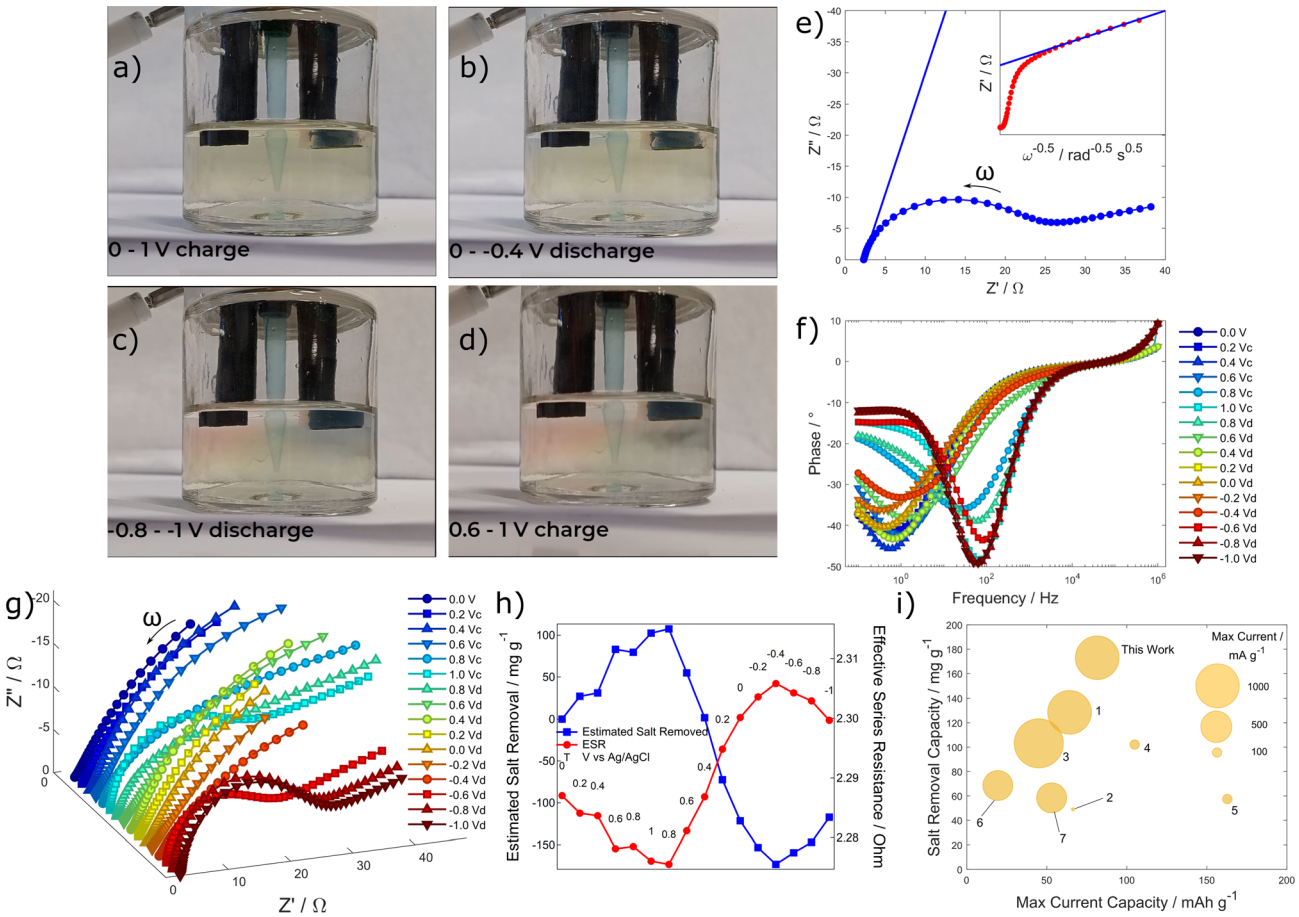

Fig. 6 (a–d) Display the desalination cell in action with universal indicator added. Potentiostatic EIS was performed at a range of different DC potentials to measure the solution resistance (Effective Series Resistance, ESR) by the intercept with the *x*-axis, and the diffusion coefficient was determined by plotting the real resistance *versus* angular frequency $\omega^{-1/2}$ (inset, e). The Bode plots at all the DC voltages measured in sequence and 3D Nyquist plots are shown in s (f and g), respectively. The estimated mass of salt removed and the ESR are shown in (h) at the various DC potentials. Finally, a comparison of literature-reported charge capacity *versus* salt removal capacity is shown in (i), for (symbol [reference]) 1 (ref. 24), 2 (ref. 46), 3 (ref. 25), 4 (ref. 47), 5 (ref. 48), 6 (ref. 49), 7 (ref. 50).

Fig. S16. Diffusion coefficients were calculated from the linear fit of the low-frequency plot of $\omega^{-1/2}$ against Z' (shown in the inset of Fig. 6e), and details of the calculation are included in the SI.[51]

The slight changes in ESR were attributed to distinct changes in solution resistivity resulting from the extraction of Na^+ and Cl^- ions through charging, as shown in Fig. 6h. During the open circuit to 1 $V_{Ag/AgCl}$ charge, the ESR decreased from 2.287 to 2.276 ohm, as expected, as Na^+ is extracted from the NVOH. This trend is reversed as the DC potential was reduced from 1 to −0.4 $V_{Ag/AgCl}$, solution resistance increasing to 2.306 ohm, 19 mohm greater than the initial value. This coincides with the reduction peak in the CV traces (Fig. 5), indicating a maximum sodium storage at this event. Resistance increases beyond this point, likely due to the generation of acidic and basic species through electrolysis. The values for ESR were subsequently converted to conductivity, using a geometric factor based on the area of the working electrode ($A = 1.13$ cm^2) and the effective ionic path length (EIPL 0.36 cm, calculated to ensure the open circuit was calibrated to the value measured by a conductivity meter, 131.7 mS cm^{-1}). The multiplication of A by the EIPL gave the effective ionic volume V as the localised volume of electrolyte in the cell where ions were extracted. The conductivity S (μS cm^{-1}) was first converted to total dissolved salts, TDS (mg kg^{-1}), by the following equation (conversion factor k was assigned as 0.64) [52]

$$\mathrm{TDS} = kS$$

Desalination capacity σ_{NaCl} ($\mathrm{mg_{NaCl}\ g^{-1}}$) was calculated using the TDS values for initial and final concentrations, C_0 and C_f, respectively:

$$\sigma_{\mathrm{NaCl}} = \frac{V(C_f - C_0)}{m}$$

where m is the active mass of material of the electrode in g.[21] Using this methodology the following values of salination/desalination capacity for NVOH were estimated, during charge up to 0.8 $V_{Ag/AgCl}$ 108 mg g^{-1} salination capacity was calculated. Upon discharge to −0.4 $V_{Ag/AgCl}$ a desalination capacity of 173 mg g^{-1} was determined.

This represents a highly favourable extraction of salt, relative to the highest value in the previous literature (see Fig. 6i, all literature compared is shown in Table S3), and is achieved due to the highest specific capacity at 1000 mA g^{-1}; this study highlights NVOH as one of the most effective known desalination battery electrodes. The findings also show a significant improvement over the use of Ag@rGO *versus* $Na_{1.1}V_3O_{7.9}$@rGO for electrochemical desalination, achieving σ_{NaCl} of 82.2 mg g^{-1} at a fixed potential of 1.4 V (so not being used as a desalination battery).[22] To compare the sodium extraction to the specific capacity of NVOH from sodium intercalation, the desalination capacity can be converted to a sodium extraction capacity, σ_{Na}, using the following conversion based on the relative atomic masses of Na (M_{Na}) and Cl (M_{Cl}).

$$\sigma_{Na} = \sigma_{NaCl}\frac{M_{Na}}{M_{Na} + M_{Cl}}$$

The value 173 mg g^{-1} gives a σ_{Na} value of 68 mg g^{-1}, which is near-equivalent to an additional sodium ion intercalation into NaV_3O_8 (71.9 mg g^{-1}), during its reduction.

This work presents a flexible system for screening new materials for electrochemical desalination, eliminating the need for the large active area and complex membrane-flow assembly typically required in alternative approaches. Notably, the solution conductivity in such an approach exhibits measurable and reproducible changes, enabling a useful comparison. When compared to electrode materials in alternative desalination batteries, NVOH (at 1000 mA g^{-1} capacity) outperforms all others reviewed at 1000 mA $g_{NVOH}{}^{-1}$ in terms of salt extraction, and also outperforms many reported materials at lower current densities. Overall, this result highlights NVOH as one of the most effective sodium storage electrodes for desalination applications. This testing platform represents a step change in the low-cost identification and screening of new aqueous batteries and desalination materials.

Conclusion

This study applies hydrated NVOH as an electrode material in organic medium sodium-ion batteries and in aqueous desalination cells. Physical characterisation revealed insights on the evolution of structure, morphology and reaction mechanism up to 48 h of hydrothermal synthesis; 24 h was shown to be sufficient to fully sodiate the sample and greater water uptake was measured at longer durations (due to long-time hydration of interlayer sodium ions).

The increased interlayer spacing resulting from crystal water and a high level of sodiation led to greatly improved low current charge storage capacity (280 mA h g^{-1}, 10 mA g^{-1}), while maintaining a higher diffusion coefficient relative to the sample with the greatest H_2O content. Promising specific capacities within idealised half cells yielded high performance in full cells made against C@V_2O_3 anodes for 70 mA h g^{-1} and greater than 100 W h kg^{-1} based on the active material mass.

When applied to a three-electrode, high-volume desalination cell in NaCl (aq, 3 mol dm^{-3}), NVOH at 1000 mA g^{-1} leads to a remarkable specific charge capacity of 81.5 mA h g^{-1}, with a 1000 cycle capacity of 25.3 mA h g^{-1}. This work brings hydrated sodium vanadium oxides to the fore as outstanding and versatile sodium storage materials.

Author contributions

Daniel Commandeur: funding acquisition, conceptualisation, investigation, validation, visualisation, software, writing – original draft. Vlad Stolojan: investigation and resources. Monica Felipe-Sotelo: resources and writing – review & editing. David Watson: investigation of scale up. James Wright: analysis and model fitting of XRD data. Robert C. T. Slade: resources, supervision (mentorship) and writing – review & editing.

Conflicts of interest

The authors declare no conflicts of interest.

Data availability

The data supporting this article have been included as part of the SI. This data includes additional SEM images, measured geometric distributions of the powder, Pawley refinement of XRD data, XPS survey data with surface carbon content, derivative heat flows from TGA, electrochemical calculations, half-cell CVs, GITT curves with diffusion coefficients, GCD capacity voltage plots, and the results of scale-up synthesis. It also includes the calculation of vanadium ionisation state and sodium content, CV data from aqueous cells, alternative efficiency calculations, diffusion coefficients, and a literature review of desalination batteries. See DOI: **https://doi.org/10.1039/d5ta05128b**.

Acknowledgements

The authors thank both the University of Surrey and the Royal Society (grant code RG\R1\251473) for their support of this study.

References

1 A. M. Abdalla, M. F. Abdullah, M. K. Dawood, B. Wei, Y. Subramanian, A. T. Azad, S. Nourin, S. Afroze, J. Taweekun and A. K. Azad, *J. Energy Storage*, 2023, **67**, 107551.
2 H. Ding, H. Li, Q. Tao, J. Ren and J. He, *ACS Appl. Nano Mater.*, 2024, **7**, 243–252.
3 J. He, A. Bhargav, L. Su, J. Lamb, J. Okasinski, W. Shin and A. Manthiram, *Nat. Energy*, 2024, **9**, 446–456.
4 X. Liang, T.-Y. Yu, H.-H. Ryu and Y.-K. Sun, *Energy Storage Mater.*, 2022, **47**, 515–525.
5 J. Zhou, Y. Zhang, W. Xu, X. Li, W. Zhou, W. Zhang, N. Wang, M. Liu and K. Dai, *J. Electroanal. Chem.*, 2024, **969**, 118541.
6 F. M. Maddar, D. Walker, T. W. Chamberlain, J. Compton, A. S. Menon, M. Copley and I. Hasa, *J. Mater. Chem. A*, 2023, **11**, 15778–15791.

7 S. Roberts and E. Kendrick, *Nanotechnol. Sci. Appl.*, 2018, **11**, 23–33.
8 S. Yuan, Y. Zhao and Q. Wang, *J. Alloys Compd.*, 2016, **688**, 55–60.
9 C. Deng, S. Zhang, Z. Dong and Y. Shang, *Nano Energy*, 2014, **4**, 49–55.
10 E. Adamczyk, M. Gnanavel and V. Pralong, *Materials*, 2018, **11**, 1021.
11 A. Vedpathak, T. Shinde, M. A. Desai, B. R. Thombare, R. Humane, S. A. Raut, R. Kalubarme, S. D. Sartale and S. Bhagwat, *ACS Appl. Energy Mater.*, 2023, **6**, 4693–4703.
12 P. Naskar, S. Debnath, B. Biswas, S. Laha and A. Banerjee, *ACS Appl. Energy Mater.*, 2023, **6**, 4604–4617.
13 W. Avansi, C. Ribeiro, E. R. Leite and V. R. Mastelaro, *Mater. Chem. Phys.*, 2011, **127**, 56–61.
14 J. Han, S. Gao, Z. Sun, Z. Yang, X. Liu and C. Wang, *Adv. Energy Mater.*, 2024, **14**, 2401481.
15 Y. Cao, J. Wang, X. Chen, B. Shi, T. Chen, D. Fang and Z. Luo, *Mater. Lett.*, 2019, **237**, 122–125.
16 S. Osman, S. Zuo, X. Xu, J. Shen, Z. Liu, F. Li, P. Li, X. Wang and J. Liu, *ACS Appl. Mater. Interfaces*, 2021, **13**, 816–826.
17 H. Wang, W. Wang, Y. Ren, K. Huang and S. Liu, *J. Power Sources*, 2012, **199**, 263–269.
18 M. J. Vujković, D. Mladenović, M. Milović, T. Petrović, D. Bajuk-Bogdanović, B. Šljukić Paunković and S. Mentus, *Electrochim. Acta*, 2022, **425**, 140603.
19 United Nations, SDG 6, **http://www.un.org/sustainabledevelopment/summit/**, accessed 6 June 2025.
20 E. Bevacqua, O. Rakovec, D. L. Schumacher, R. Kumar, S. Thober, L. Samaniego, S. I. Seneviratne and J. Zscheischler, *Nat. Geosci.*, 2024, **17**, 1100–1107.
21 F. Chen, Y. Huang, L. Guo, L. Sun, Y. Wang and H. Y. Yang, *Energy Environ. Sci.*, 2017, **10**, 2081–2089.
22 Z. Yue, Y. Ma, J. Zhang and H. Li, *J. Mater. Chem. A*, 2019, **7**, 16892–16901.
23 F. Chen, Y. Huang, L. Guo, M. Ding and H. Y. Yang, *Nanoscale*, 2017, **9**, 10101–10108.
24 Y. Wu, Q. Zou, C. Li and W. Wang, *Chem. Eng. J.*, 2024, **480**, 147965.
25 L. Guo, Y. Shang, G. Wang, J. Jin, Z. Y. Leong, S. Huang, C. Gu, M. Ding, M. E. Pam, S. Vafakhah, X. L. Li, S. A. Yang and H. Y. Yang, *J. Mater. Chem. A*, 2021, **9**, 7216–7226.
26 Y. Lyu, P. Mollik, A. L. Oláh and D. P. Halter, *ChemElectroChem*, 2024, **11**, e202300792.
27 R. Barlag, F. Nyasulu, R. Starr, J. Silverman, P. Arthasery and L. McMills, *J. Chem. Educ.*, 2014, **91**, 766–768.
28 W. Zhang, G. Xu, L. Yang and J. Ding, *RSC Adv.*, 2016, **6**, 5161–5168.
29 A. Jain, S. P. Ong, G. Hautier, W. Chen, W. D. Richards, S. Dacek, S. Cholia, D. Gunter, D. Skinner, G. Ceder and K. A. Persson, *APL Mater.*, 2013, **1**(1), 011002.
30 A. Jain, S. P. Ong, G. Hautier, W. Chen, W. D. Richards, S. Dacek, S. Cholia, D. Gunter, D. Skinner, G. Ceder and K. A. Persson, *APL Mater.*, 2013, **1**, 011002.
31 M. K. Horton, P. Huck, R. X. Yang, J. M. Munro, S. Dwaraknath, A. M. Ganose, R. S. Kingsbury, M. Wen, J. X. Shen, T. S. Mathis, A. D. Kaplan, K. Berket, J. Riebesell, J. George, A. S. Rosen, E. W. C. Spotte-Smith, M. J. McDermott, O. A. Cohen, A. Dunn, M. C. Kuner, G.-M. Rignanese, G. Petretto, D. Waroquiers, S. M. Griffin, J. B. Neaton, D. C. Chrzan, M. Asta, G. Hautier, S. Cholia, G. Ceder, S. P. Ong, A. Jain and K. A. Persson, *Nat. Mater.*, 2025, 1–11.
32 M. B. Smirnov, E. M. Roginskii, K. S. Smirnov, R. Baddour-Hadjean and J.-P. Pereira-Ramos, *Inorg. Chem.*, 2018, **57**, 9190–9204.
33 J. Chen, Y. Zhai, Y. Li, X. Zhang, X. Zhang, Y. Chen, Y. Zeng, X. Wu, Q. Zheng, K. Lam, X. Tan and D. Lin, *Small*, 2024, **20**, 2309412.
34 Y. Cao, D. Fang, X. Liu, Z. Luo, G. Li, W. Xu, M. Jiang and C. Xiong, *Compos. Sci. Technol.*, 2016, **137**, 130–137.
35 Z. Tong, R. Yang, S. Wu, D. Shen, T. Jiao, K. Zhang, W. Zhang and C.-S. Lee, *J. Mater. Chem. A*, 2019, **7**, 19581–19588.
36 X. Song, X. Li, H. Shan, J. Wang, W. Li, K. Xu, K. Zhang, H. M. K. Sari, L. Lei, W. Xiao, J. Qin, C. Xie and X. Sun, *Adv. Funct. Mater.*, 2024, **34**, 2303211.
37 J. Song, L. Wang, Y. Lu, J. Liu, B. Guo, P. Xiao, J.-J. Lee, X.-Q. Yang, G. Henkelman and J. B. Goodenough, *J. Am. Chem. Soc.*, 2015, **137**, 2658–2664.
38 B. Xie, L. Wang, J. Shu, X. Zhou, Z. Yu, H. Huo, Y. Ma, X. Cheng, G. Yin and P. Zuo, *ACS Appl. Mater. Interfaces*, 2019, **11**, 46705–46713.
39 Y. You, H.-R. Yao, S. Xin, Y.-X. Yin, T.-T. Zuo, C.-P. Yang, Y.-G. Guo, Y. Cui, L.-J. Wan and J. B. Goodenough, *Adv. Mater.*, 2016, **28**, 7243–7248.
40 S. Ragul, A. Prabakaran, E. Sujithkrishnan, K. Kannadasan and P. Elumalai, *New J. Chem.*, 2024, **48**, 12323–12335.
41 S. Liu, Z. Xu, L. Ren, W. Xu, Y. Liu, X. Fan, M. Luo, J. Li and J. Tong, *RSC Adv.*, 2024, **14**, 4835–4843.
42 L. Zhu, S. Xiang, M. Wang, D. Sun, X. Huang, Y. Li, Y. Tang, Z. Peng, Q. Zhang and H. Wang, *Adv. Mater.*, 2025, **37**, 2408918.
43 K. Kubota, N. Fujitani, Y. Yoda, K. Kuroki, Y. Tokita and S. Komaba, *J. Mater. Chem. A*, 2021, **9**, 12830–12844.
44 J. Han, S. Gao, Z. Sun, Z. Yang, X. Liu and C. Wang, *Adv. Energy Mater.*, 2024, **14**, 2401481.
45 W. Zhao, L. Guo, M. Ding, Y. Huang and H. Y. Yang, *ACS Appl. Mater. Interfaces*, 2018, **10**, 40540–40548.
46 D.-H. Nam, M. A. Lumley and K.-S. Choi, *Chem. Mater.*, 2019, **31**, 1460–1468.
47 W. Zhao, L. Guo, M. Ding, Y. Huang and H. Y. Yang, *ACS Appl. Mater. Interfaces*, 2018, **10**, 40540–40548.
48 F. Chen, Y. Huang, L. Guo, M. Ding and H. Y. Yang, *Nanoscale*, 2017, **9**, 10101–10108.
49 F. Chen, Y. Huang, L. Guo, L. Sun, Y. Wang and H. Y. Yang, *Energy Environ. Sci.*, 2017, **10**, 2081–2089.
50 W. Wei, X. Feng, R. Wang, R. Zheng, D. Yang and H. Chen, *Nano Lett.*, 2021, **21**, 4830–4837.
51 D. Commandeur, C. Sabado, T. E. Ashton and J. A. Darr, *J. Materiomics*, 2022, **8**, 437–445.
52 A. F. Rusydi, *IOP Conf. Ser. Earth Environ. Sci.*, 2018, **118**, 012019.

